Modeling of Hybrid Henry Gas Solubility Optimization Algorithm with Deep Learning based LED Driver System

Fayaz Ahamed (fayazahamedresearchscholar@gmail.com)
Y. Sukhi

Research Article

Keywords: LED Driver, Deep learning, Thermal mechanical loading, Henry gas solubility optimization, Spectral power distribution

Posted Date: January 10th, 2023

DOI: https://doi.org/10.21203/rs.3.rs-2449840/v1

Additional Declarations: No competing interests reported.

Modeling of Hybrid Henry Gas Solubility Optimization Algorithm with Deep Learning based LED Driver System

[1,*]Fayaz Ahamed A, [2]Dr.Y.Sukhi

[1,*]Assistant Professor, Department of EEE, R.M.K Engineering College,

[2]Professor, Department of EEE, R.M.K Engineering College,
[2]ysi.eee@rmkec.ac.in
[1,*]fayazahamedresearchscholar@gmail.com

Abstract

Light emitting diodes (LED) become an effective lighting solution because of the characteristics of energy efficiency, flexible controllability, and extended lifetime. They find use in numerous lighting systems for residents, industries, enterprises, and street lighting applications. The efficiency and trustworthiness of the LED systems considerably based on the thermal mechanical loading improved several degradation schemes and respective interfaces. The complication of the LED systems limits the theoretic interpretation of the core reasons for the luminous variation or the formation of the direct correlation among the thermal aging loading and the luminous output. Therefore, this article designs a new Hybrid Henry Gas Solubility Optimization with deep learning (HHGSO-DL) algorithm for LED driver system design. The presented HHGSO-DL technique mainly concentrates on the derivation of empirical relationships among the design parameters, thermal aging loading, and luminous outcomes of the LED product. In the presented HHGSO-DL technique, bidirectional long short-term memory (BiLSTM) algorithm is executed for examining the empirical relationship and its hyperparameters can be tuned by the HHGSO algorithm. In this work, the HHGSO algorithm is derived by the integration of traditional HGSO algorithm with oppositional based learning (OBL) concept. The performance of the HHGSO-DL technique can be investigated on LED chip packaging and LED luminaire with thermal aging loading. The extensive results demonstrate the promising performance of the HHGSO-DL technique over other state of art approaches.

Keywords: LED Driver; Deep learning; Thermal mechanical loading; Henry gas solubility optimization; Spectral power distribution

1. Introduction

Power LEDs were the most effective light source in the marketplace, and it has lifetime. Power

LEDs were utilized in many lighting mechanisms, like street lighting, suburban enterprise, and industrial applications [1]. LED driver utilizes dc-dc converters for maintaining constant LED current since it is destructed when an overcurrent circulated over them. Nowadays, power LED-driver mechanism operates through power converter namely dc-dc converter [2] that was utilized for attaining a constant LED current due to power LEDs. In some cases, such variations can end them [3]. Hence a LED driver related to dc-dc converters was needed for controlling LED current as LEDs have higher sensitivity to voltage variations are criteria that cause current to make a great increase in value if the volt has smaller changes. LED drivers related to buck converters with constant on-time control loops were provided, and optimum outcome in the LED current control was attained [4]. The LED chip has a lifespan of as long as 25 000– to 1,00,000 h, while LED or system lamps include a short life. Nowadays, it is noted that there were several mechanical failures to cause rapid deprivation of LEDs mechanism. The water in silicone causes bubble generation [5]. The high temperature at silicone or phosphor interface may cause cracking, discolorations, and decohesion of interface layer. One more study shows that including phosphor with higher temperature aging will stiffen silicone matrix. Fig. 1 shows the LED system with its packaging.

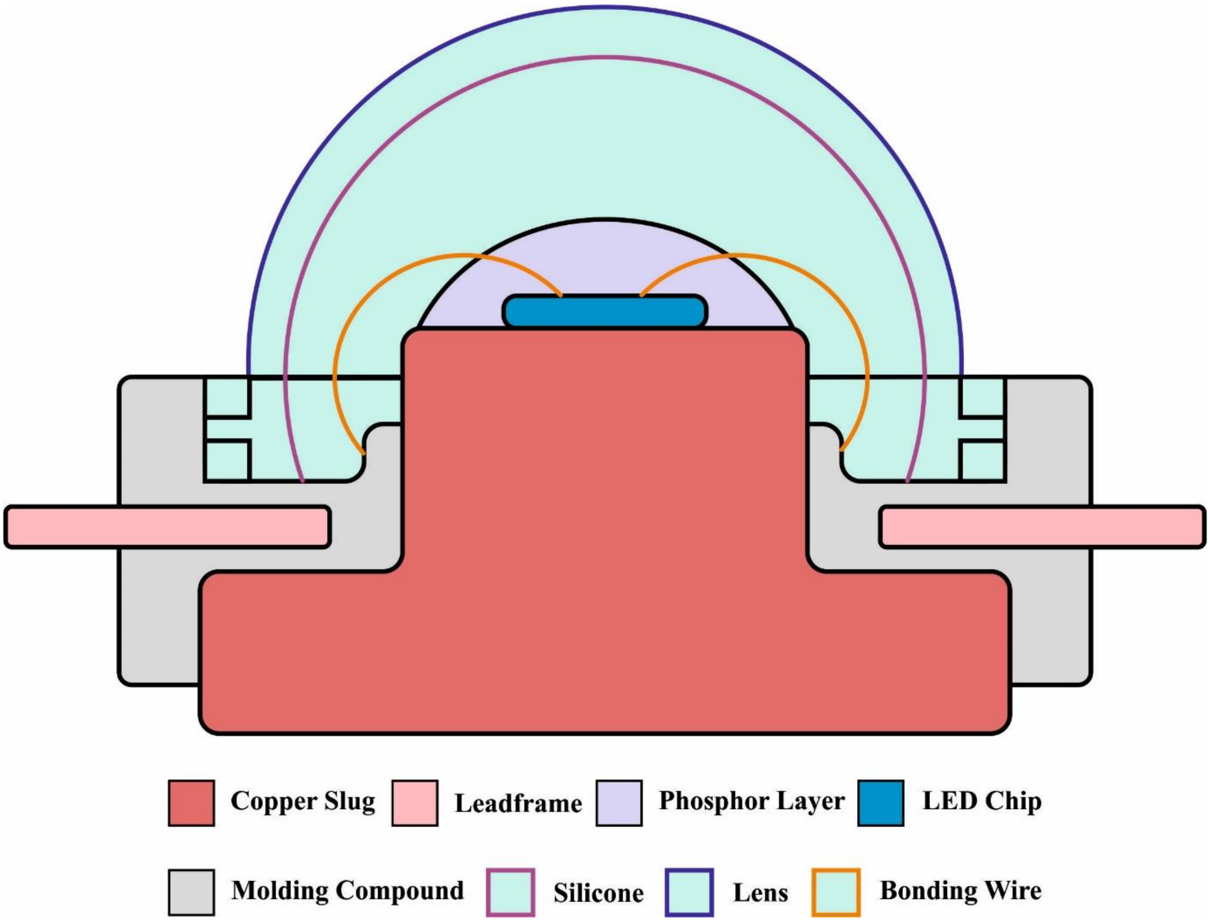

Fig. 1. LED system with its packaging [22]

The thermal dissipation design had a play a vital role [6]. Additionally, the LEDs driver, which was highly complex system in an LED lamp, has an important effect on performance of the LEDs, since driver regulated the electric current inputs for LED mechanism [7]. Several research works have engrossed in investing systems or systems for degrading LED mechanisms. For instance, a physics-of-failure-related reliability predictive method for LED drivers was formulated for estimating failure rate distribution of electrolytic capacitors of a given LEDs driver mechanism [8]. The electronic–thermal simulation was taken place to study the relation among driver's luminous flux and output current. Currently, a complete study has been held for investigating the impact of phosphor and humidity on moisture absorption, mechanical behavior, hygroscopic swelling, and thermal properties of silicone composite compared to pure silicone [9]. Recently, the machine learning (ML) technique was broadly utilized in different research fields. It was proved that manages the complexities with high multivariate relationships and nonlinearity. In the domain of electronic packaging, for renowned failure systems [10].

This article focuses on the development of Hybrid Henry Gas Solubility Optimization with deep learning (HHGSO-DL) algorithm for LED driver system design. The presented HHGSO-DL technique aims to derive the empirical relationship among design parameters, thermal aging loading, and luminous outcomes of the LED product. In the presented HHGSO-DL technique, bidirectional long short-term memory (BiLSTM) method can be utilized to examine the empirical relationship and its hyperparameters can be tuned by the HHGSO algorithm. In this work, the HHGSO algorithm is derived by the integration of traditional HGSO algorithm with oppositional based learning (OBL) concept. The experimental result analysis of the HHGSO-DL technique can be inspected on LED chip packaging and LED luminaire with thermal aging loading.

2. Related Works

In [11], the fractional-order system was explained with respect to El-Khazali biquadratic element that creates the low-order estimate, rather than utilizing a description. A 2-mode controller infrastructure was synthesized based on uncontrolled plant requirements and parameter is modified with PSO and GA techniques for evaluation. Two error-based minimized conditions can be utilized for considering outcome efficacy in the procedure. The 2 limitations complement the optimized approach, one searches for ensuring preferred robustness but the other avoids in synthesized a higher-gain controller. Xu et al. [12] examine an offset-free method forecast controller to dc/dc buck converter providing constant power load with assured dynamic efficacy and stability. Primarily, a receding horizon optimized (RHO) technique was expressed to better voltage tracking. For handling unknown load variation and scheme uncertainty, a high-order sliding approach observer was planned and combined as optimized challenge. Afterward, an explicit closed-loop solution was attained by resolving the RHO technique offline.

Kreiss et al. [13] introduce a control technique for parallel interconnection of heterogeneous power converters. The single resistive load was considered that provided by random count of buck converters using general DC bus. This technique was dependent upon control allocation method and a constrained quadratic optimizes system. In [14], a new approach for tuning fractional order controller (FOC) named fractional order pole placement (FOPP) was presented. The presented technique extends typical (integer order) pole placement approach, utilizing commensurable transfer function to signify FOC and locating the fractional dominant pole in extended stability area dependent upon 3 terms fractional transfer functions. The presented FOPP was utilized for designing FOC for DC-DC buck converters.

Zhang et al. [15] examine the subsea high voltage DC/DC converters (HVC) that highly enhance the power and voltage levels of underwater observation networks. The typical series-parallel converter is dependent upon multi-module and deals with several technical issues like several fault points, complex transformer isolation, superior output power, and lower power density in maximum input voltage level. The underwater HVC of this work implements modular multi-level resonant DC/DC converters. The authors [16] present a single-stage IPT converter for battery charge level. Through a constant working frequency and without feedback wireless transmission, receiver side directly controls the resultant for complying with CC-CV charging profile, but the receiver side supports the decrease of modulated phase shift angle at transmitter side, so enhancing performance. In addition, the authors execute implicit a resultant voltage regulation, avoiding require of extra dc–dc converters.

Liao et al. [17] present an optimizing parallel virtual resistance (PVR) related active damping control for improving the constancy of cascades dc method from the dc micro-grid. The benefit of this technique is not only occurring the closed-loop dynamic result of source converters (SC), among them occurs the stability necessities of equivalent input impedance of load converters. In [18], a new approach for non-linear and adaptive control of bucks DC-DC converter was projected. Even though an extensive load variation, presented controller was able of regulates resultant voltage from Discontinuous Conduction Mode (DCM) and Continuous Conduction Mode (CCM).

3. The Proposed Model

In this study, we have developed a new HHGSO-DL technique for LED driver system design. The presented HHGSO-DL technique is majorly intended the determination of the empirical relationship among the design parameters, thermal aging loading, and luminous outcomes of the LED product. In the presented HHGSO-DL technique, the HHGSO with BiLSTM model can be employed to examine the empirical relationship and its hyperparameters can be tuned by the HHGSO algorithm. Fig. 2 shows the derivation of the presented S6- PFC LED driver by incorporating a buck-boost converter with the mentioned single-switch soft-switched resonant DC-DC converter [10]. The resonant converter utilizes a unidirectional switch operating under ZCS condition. These converters can be integrated such that both of them share a common switch. Since in the integrated structure, currents of both converters flow through the common switch, its ZCS turn-off condition is lost.

3.1. System Modeling

The LED-driver model was generally a non-linear mechanism. The state-space averaging modeling technique was utilized as a replacement for state-space switching method since it facilitated the model of control stages [19]. Depending on after mentioned words, and by utilizing the schematic diagram of LED-driver mechanism nonlinear state-space averaged mechanism method is given below:

$$\dot{x}(t) = Ax(t) + Bu(t) + P, \tag{1}$$

$y(t) = \Gamma x(t),$

with

$$A = \begin{bmatrix} 0 & -\frac{1}{L} \\ \frac{1}{C} & -\frac{1}{CR_y} \end{bmatrix}, B = \begin{bmatrix} \frac{E}{L} \\ 0 \end{bmatrix}, P = \begin{bmatrix} 0 \\ \frac{V_y}{CR_y} \end{bmatrix}, \Gamma = [1 \quad 0], \tag{2}$$

Here $x(t) = [x_1(t), x_2(t)]^T = [i_L(t), v_C(t)]^T \in \mathbb{R}^n$ signifies the state vector, signified by the inductor current and capacitor voltage, with $n = 2$. The resultant vector was provided by $y(t)$.

In order to track control design, it considers the outcome is only $i_L(t)$. For controlling LED driver, the dynamic mechanism (1) can be discretization through the Euler technique. Then the following mechanism can be attained:

$$x(k+1) = A_d x(k) + B_d u(k) + P_d, \tag{3}$$

$$y(k) = \Gamma_d x(k),$$

with

$$A_d = \begin{bmatrix} 0 & -\dfrac{T_s}{L} \\ \dfrac{T_s}{C} & -\dfrac{T_s}{CR_y} + 1 \end{bmatrix}, B_d = \begin{bmatrix} \dfrac{ET_s}{L} \\ 0 \end{bmatrix}, P_d = \begin{bmatrix} 0 \\ \dfrac{V_y T_s}{CR_y} \end{bmatrix}, \Gamma_d = [1 \quad 0], \tag{4}$$

Here T_s signifies the sample time.

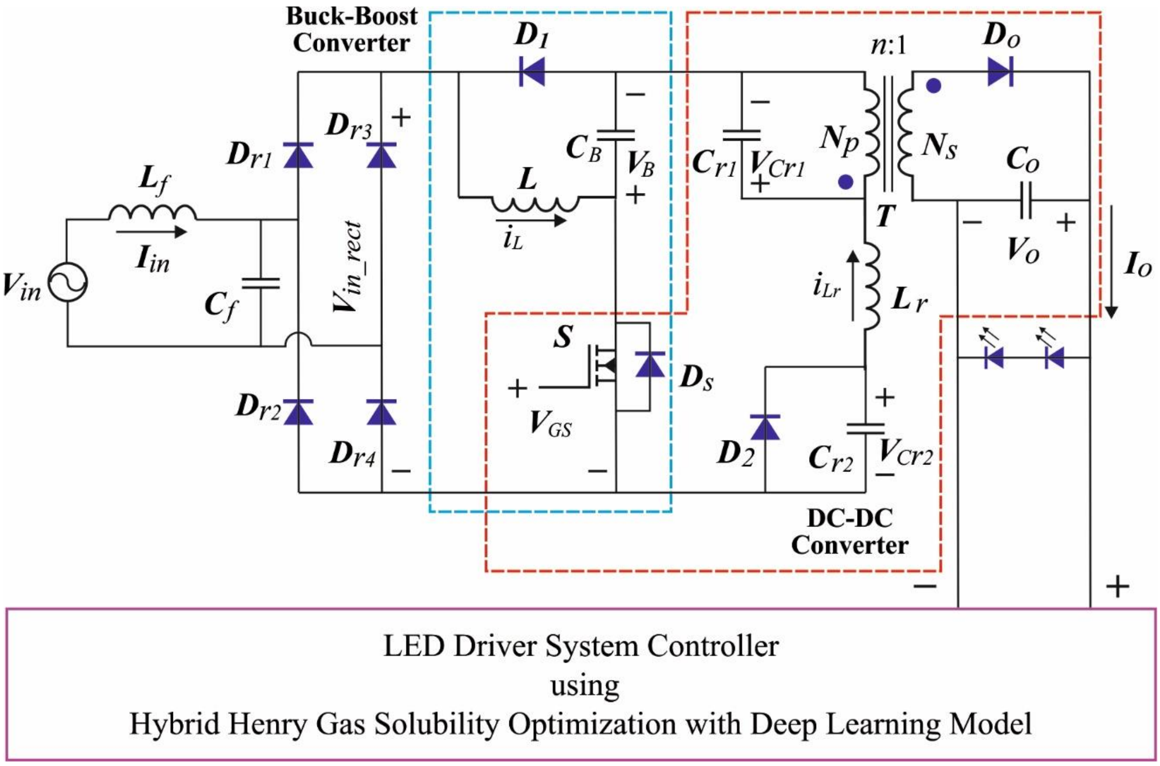

Fig. 2. Circuit topology and derivation of the proposed LED driver [10]

3.2. Design of BiLSTM Model

In this work, the HHGSO-DL technique exploits the BiLSTM model for the identification of empirical relationships between the design parameters. Hochreiter and schmidhuber developed an LSTM mechanism which is adapted version of RNN [20]. It can be considered as RNN's long-term memory of historical data, and avoid gradient disappearing problems of RNN by substituting recurrent hidden layers (HLs) in RNN with ‘memory blocks’. Due to the ‘memory block’ presented in LSTM, the LSTM was considered as the forward propagation chain structure as follows:

The input of LSTM denoted as $= (x_1, x_2, \ldots, x_T)$, and the target output as $y = (y_1, y_2, \ldots, y_T)$, the targeted output y_t at t time is evaluated based on the subsequent steps:

(1) Calculate forget gate f_t:

$$f_t = \sigma\left(W_f \cdot [h_{t-1}, x_t] + b_f\right) \tag{5}$$

(2) Calculate input gate:

$$i_r = \sigma(W_i \cdot [h_{t-1}, x_t] + b_i) \tag{6}$$

$$C_r' = tanh(W_c \cdot [h_{t-1}, x_t] + b_c) \tag{7}$$

(3) Upgrade cell state:

$$C_t = f_t * C_{t-1} + i_t * C_t' \tag{8}$$

(4) Calculate output gate:

$$O_t = \sigma(W_o[h_{\mathrm{t}-1}, x_{t-1}] + b_o) \tag{9}$$

$$h_t = O_{\mathrm{t}} * tanh(C_t) \tag{10}$$

(5) Calculate predicted value y_t:

$$y_t = W_y h_t + b_y \tag{11}$$

Where i_t and C': resides the input gates,

C_f and C_{r-1}: represent present and prior cell state, correspondingly;

O_t and h_t: indicates the output gate and the outcome of h_t HL for present period is attained;

W_f, W_i, W_c, W_o and W_y: denotes the weight matrix for forgetting gate, input gate, present cell state, output gate, and output layer, correspondingly;

b_f, b_c, b_o and b_y: symbolize the equivalent bias vector;

$\sigma(x)$ and tanh (x): signify Sigmoid and Tanh activation functions, correspondingly and it is formulated by:

$$\sigma(x) = \frac{1}{1+e^{-x}} \tag{12}$$

$$tanh(x) = \frac{e^{\chi} - e^{-x}}{e^{\chi} + e^{-x}} \tag{13}$$

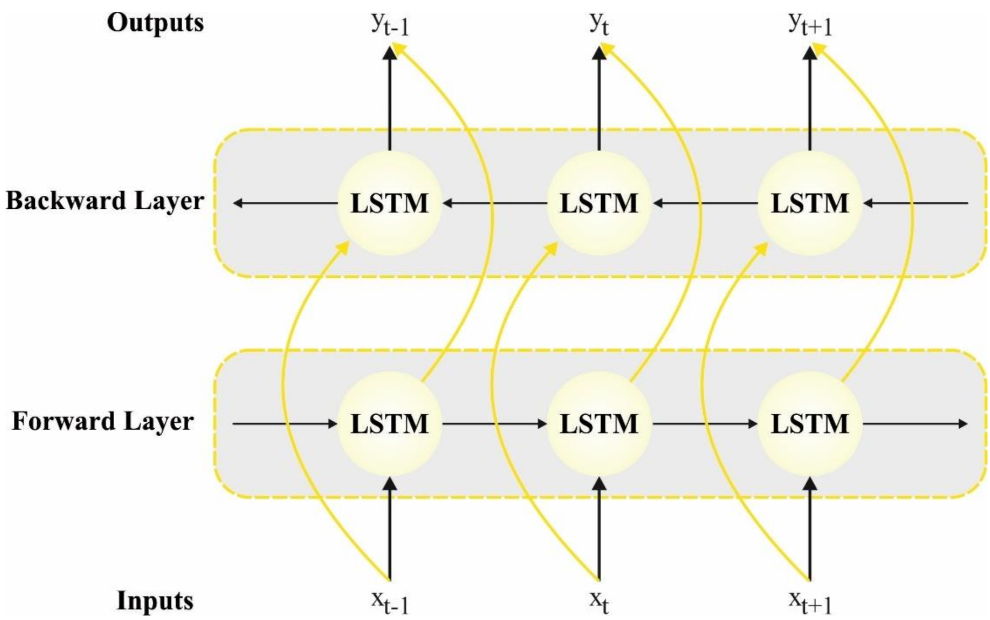

Fig. 2. Framework of BiLSTM

BLSTM is a deformation configuration of LSTM that has forward as well as backward LSTM layers. The BLSTM simultaneously considers historical and upcoming information. Fig. 2 defines the infrastructure of BiLSTM. The structure of BLSTM-NN has been demonstrated. Every memory block has 2 LSTM layers. By using the forward LSTM layer S_f, $t \in [1, \mathrm{T}]$ and the backward LSTM layer S_r', $t \in [T, 1]$, 2 HLs with opposite time sequence was attained. Later, the 2 HL states are interconnected for getting a similar outcome. The forward and backward LSTM layers could attain the previous and future data of an input sequence, correspondingly. The HL state H_t of BLSTM at t time has $\overrightarrow{h_t}$ forward and $\overleftarrow{h_t}$ backward:

$$\overrightarrow{h_t} = \overrightarrow{LSTM}(h_{t-1}, x_t, c_{t-1},), \mathrm{t} \in [1, T] \tag{14}$$

$$\overleftarrow{h_t} = \overleftarrow{LSTM}(h_{t+1}, x_t, c_{t+1}\ r \in [T, 1] \tag{15}$$

$$H_t = [\overrightarrow{h_t}, \overleftarrow{h_t}] \tag{16}$$

Whereas T indicates the length of time series.

3.3. Algorithmic Design of HHGSO Algorithm for Parameter Optimization

For enhancing the efficiency of the BiLSTM model, the HHGSO algorithm can be used as hyperparameter optimizer. HGSO algorithm is based on the solubility behaviors of gas in the fluid according to Henry's law which is inversely proportional to the corresponding gas pressure and temperature [21]. Henry's law can be mathematically formulated using below equation where S_g corresponds to the solubility of the gas:

$$S_g = H \times P_g \tag{17}$$

In Eq. (17), H indicates Henry's constant, and P_g characterizes the partial pressure of the gases. The relationship between the temperature dependence and Henry's constant of the algorithm is defined using the Van't Hoff formula:

$$\frac{d \ln H}{d(l/T)} = \frac{-\nabla_{sol} E}{R} \tag{18}$$

In Eq. (18), $\nabla_{sol}E$ denotes the enthalpy of dissolution, R shows the gas constant, and A and B represent two variables for T that rely on H. According to the Van't Hoff formula, Eq. (17) is simplified below:

$$H(T) = \exp\left(\frac{B}{T}\right) \times A \tag{19}$$

In Eq. (19), H indicates the A and B parameter function for T dependence of H. On the other hand, it is possible to create a formulation according to H^{θ} at the reference temperature $T = 298.15$ K.

$$H(T) = H^0 \times \exp\left(\frac{-\nabla_{so1} E}{R}\left(\frac{1}{T} - \frac{1}{T^{\theta}}\right)\right) \tag{20}$$

Since the Van't Hoff equation is valid once $\nabla_{so1}E$ denotes a constant, Eq. (20) is formulated by:

$$H(T) = \exp\left(-C \times \left(\frac{1}{T} - \frac{1}{T^{\theta}}\right)\right) \times H^{\theta} \tag{21}$$

As abovementioned, the HGSO technique is explained in eight stages as shown below:

Step1: Initialization process. The position of N number of gases is initialized randomly as follows:

$$X_i(t+1) = X_{\min} + r \times (X_{\max} - X_{\min}) \tag{22}$$

In Eq. (22), t and r represent the existing count of iterations and a uniformly distributed random parameter, correspondingly. The location of i^{th} gas in population N can be symbolized as $X_{(i)}$. $X_{\max}$ and $X_{\min}$ are the maximal and minimal boundaries of the problem. $H_j(t)$, and $P_{ij}C_i$, are the Henry's constant, partial pressure, and constant for i^{th} gas and j^{th} clusters. The parameter is initialized based on Eq. (21):

$$H_j(t) = l_1 \times rand(O,1), P_{ij} = l_2 \times rand(0,1), C_j = l_3 \times rand(O,1) \tag{23}$$

where $l_1 = 5E - 02$, $l_2 = 100$, and $l_3 = 1E - 02$ are constant.

Step2: Clustering, the size of cluster is equivalent to the number of types of gases. The gas in the similar cluster has similar Henry's constant value (H_j).

Step3: Evaluation, the cluster is evaluated for finding the better gas in the respective cluster. Next, the best clusters are ranked according to the fitness value and discover the optimum gas in the whole population.

Step 4: Upgrade Henry's coefficient, H_j is modified based on below equation for j^{th} cluster and iter characterize the overall quantity of iterations:

$$H_j(t+1) = H_j(t) \times \exp\left(-C_j \times \left(\frac{1}{T(t)} - \frac{1}{T^{\theta}}\right)\right), T(t)$$

$$= \left(-\frac{t}{iter}\right) \tag{24}$$

Step5: Upgrade solubility, the HGSO modifies the solubility of i^{th}gas in cluster $j(S_{i,j})$ based on Eq. (25) where $P_{i,j}$ indicates partial pressure on i^{th} gas in j^{th} cluster and K represent a constant:

$$S_{i,j}(t) = K \times H_j(t+1) \times P_{i,j}(t) \tag{25}$$

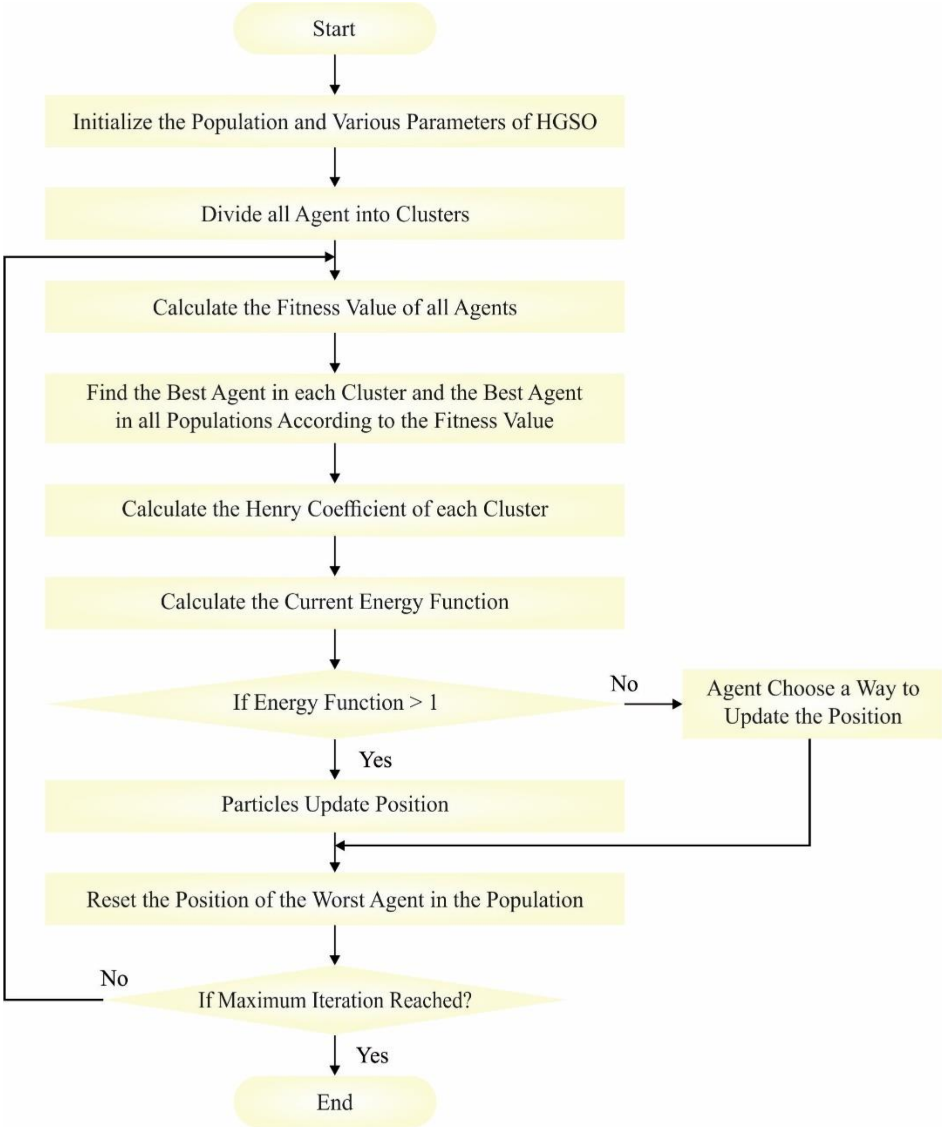

Fig. 3. Flowchart of HGSO

Step6: Upgrade location, The HGSO modify the location of i^{th} gas in cluster j ($X_{(i,j)}$) at t^{th} iterations using Eq. (24) whereby r indicates the random number.

$$X_{i,j}(t+1) = X_{i,j}(t) + F \times r \times \gamma \times \left(X_{i,best}(t) - X_{i,j}(t)\right)$$

$$+F \times r \times \alpha \times (S_{i,j}(t) \times X_{best}(t) - X_{ij}(t))$$

$$\gamma = \beta \times \exp\left(-\frac{F_{best}(t) + \varepsilon}{F_{ij}(t) + \varepsilon}\right), \varepsilon = 0.05 \quad (26)$$

X_{best} and $X_{(i,best)}$ represents the best of swarm and cluster, correspondingly that is directly accountable to controlling the exploitation and exploration phases. Furthermore, β, and γ

represent the influence of other gases on present gas, a random number, and the interaction capability of gas in a similar cluster. The fitness of i^{th} gas in j^{th} cluster is signified as $F_{(i,j)}$. On the other hand, the fitness of global optimum is represented as F_{best}. To guarantee diversity, the flag F controls the search direction.

Step7: Escape from local optimal, this step rank and chooses the amount of worst agents (N_w) by means of Eq. (27) for escaping from local optimal whereby N indicates the number of searching agents:

$$N_w = N \times (rand(c_2 - c_1) + c_1), c_1 = 0.1, c_2 = 0.2 \tag{27}$$

Step8: Upgrade the worst agent location.

$$x_{(i,j)} = X_{\min(i,j)} + r \times \left(X_{\max(i,j)} - X_{\min(i,j)}\right) \tag{28}$$

In Eq. (28), $X_{\min}$, and $X_{\max}$ represents a random value, minimum, and maximum bounds of the problem, correspondingly. Fig. 3 demonstrates the flowchart of HGSO technique.

Algorithm 1: Pseudocode of HGSO algorithm

Start
 	
Initialize population $X_i (i = 1,2, \dots, N)$, count of gas types $i, H_j, P_{\mathrm{i,j}}, C_j, l_1, l_2$ and l_3.
 	
Separate the population agents into the count of gas types (cluster) with similar Henry's constant value $\left(H_j\right)$
 	
Assess all clusters j.
 	
Get the optimal gas $X_{i,best}$ in all clusters, and the optimal search agent X_{best}.
 	
while (stopping criteria not met $(i.e.\ t < \mathrm{Max}_{iteration})$)
 	
    for all search agents do
 	
        Upgrade the location of individual search agents.
 	
    end for
 	
    Upgrade Henry's co-efficient of all gas types.

Upgrade solubility of all gas.

Rank and choose the count of worse agents.

Upgrade the location of the worse agents.

Upgrade the optimal gas $X_{i_3 besl}$, and optimal searching agent X_{best}

$t = t + 1$

end while

return X_{best}

end

The underlying HGSO technique has several shortcomings including slower convergence and easily getting trapped in local optima. This drawback arises from upgrading some solutions toward the local optimum solution even though there are more suitable and available however far away solutions that HGSO could not manage to determine. Consequently, the solution in the opposite direction is needed to be taken into account for avoiding these shortcomings. The study assists to enhance the HGSO in 2 ways. Initially, the OBL is exploited for initializing the population by exploring all the search space and accelerating the convergence for every solution to prevent stagnating in a local optimum solution. Furthermore, it can be utilized to control the upgraded solution in the opposite direction and compare the solution with the present one for checking whether there is alternative solution. Thereby, it prevents local optimum minimum. The subsequent subsection explains the stages exploited for the presented technique. The HHGSO method begins by initializing an arbitrary population of X that has size of N so that the location vector for the first solution was defined by $\mathrm{x_i} = [\mathrm{x_{i1}}, \mathrm{x_{i2}}, \cdots, \mathrm{x_{in}}]$ where $i = 1,2, \cdots, N$. Then, the OBL is exploited for calculating the solution from the opposite direction of all the solutions and produces an opposite population of $\overline{X}$. With the populations of X and $\overline{X}$, the N amount of optimum solutions is selected. During this stage, the steps are given below:

- Begin the solution for population of X randomly.
- Evaluate the opposite population of $\overline{X}$ as follows:

$\overline{x}_{ij} = u_i + l_i - x_{ij}$ whereas $i = 1,2,\cdots,N$ and $j = 1,2,\cdots,n$. Now, l and u denote the lower as well as upper bounds for the searching space, correspondingly. x_{ij} and $\overline{x}$ indicates the j^{th} solution of i^{th} location for the X population and the $\overline{X}$opposite population, correspondingly.

- Select N number of optimum solutions from the $X \cup \overline{X}$ union for creating a new population.

The better solution (x_p) can be defined (from the initial stage) afterward selecting the better N solutions. The agent in population of X are upgraded by the HGSO technique and the fitness function is evaluated. Furthermore, the opposite population of $\overline{X}$ is evaluated based on the OBL and the fitness function for every $\overline{x}$ is defined. Next, select N count of optimum solutions in the union of population$(X \cup \overline{X})$. Each step is repeated until ending criteria are attained.

4. Results and Discussion

In this section, the experimental validation of the HHGSO-DL technique is investigated briefly.

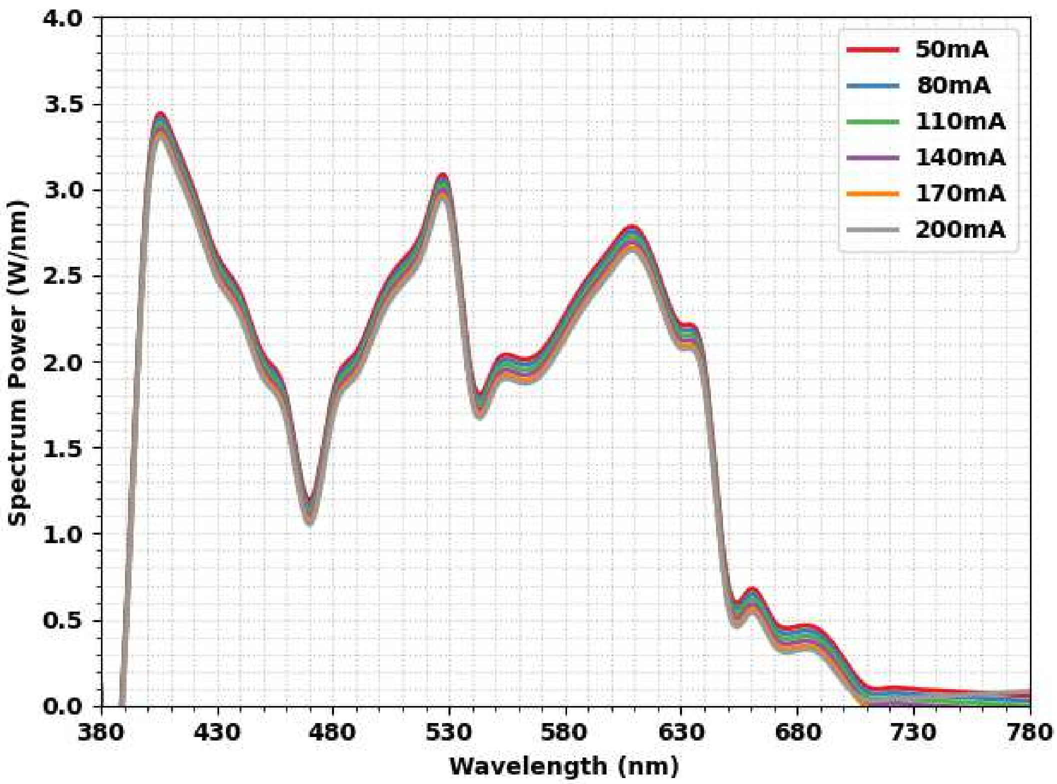

Fig. 4. Spectrum power in varying inputs current

The SPDs of the several chip packaging in several temperatures and input currents as shown in Fig. 4. The color features derivative in the SPDs. While the 3 LED chips are executed, there are 3 important peaks. The flat plateau at ~530–625nm is the influence of emission of the phosphors that is based on the blue and cyan chips. In all distinct sets of currents and temperatures, the fundamental SPD shapes could not be altered. The spectral power enhances with maximal from the input current.

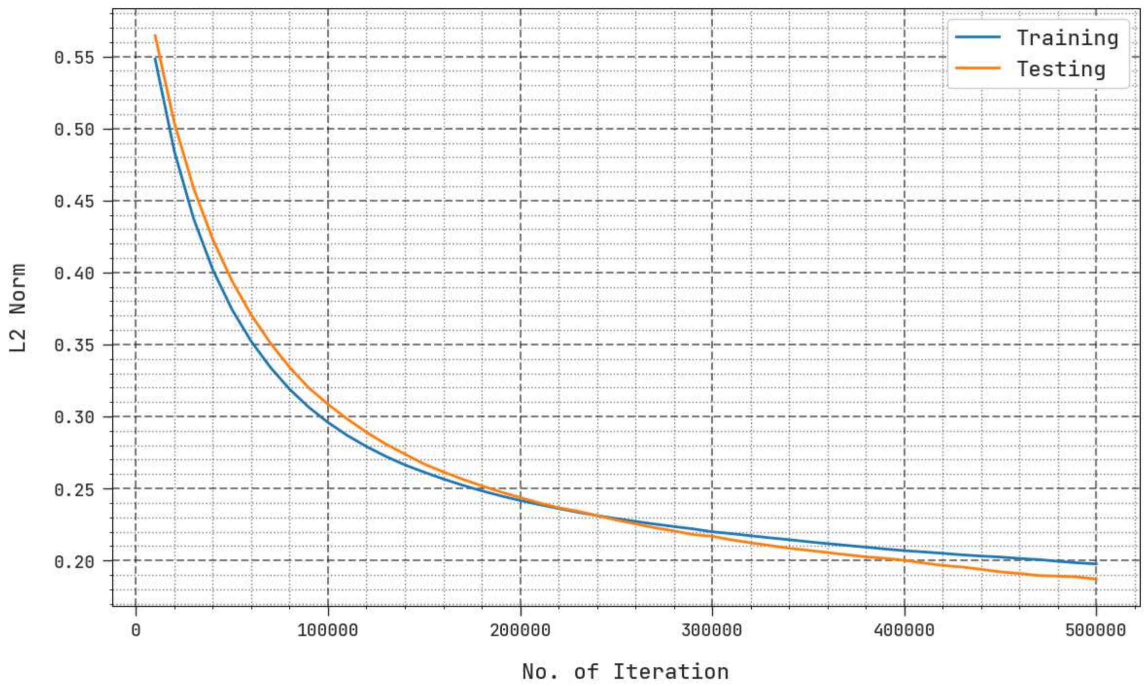

Fig. 5. Convergence Rate

Fig. 5 examines the convergence analysis of HHGSO-DL technique with varying iterations. The results inferred that the HHGSO-DL technique achieves effective convergence over several iterations. The color features obtained from the SPD are given in Table 1, comprising the correlated color temperature (CCT) and the color co-ordinate depending upon the CIE 1931 standard.

Table 1 Color features in SPD

No.	**Input current**	**Case temperature (°C)**	**CCT (K)**	**CIE *X***	**CIE *Y***
1	50mA	25	5233	0.3715	0.3510
2	50mA	40	4698	0.3349	0.3761
3	50mA	60	5334	0.3215	0.3772
4	50mA	70	5590	0.3095	0.3625
5	50mA	80	5257	0.3415	0.3659
6	80mA	25	4967	0.3517	0.3754

7	80mA	40	4895	0.3176	0.3565
8	80mA	60	4989	0.3129	0.3577
9	80mA	70	5145	0.3540	0.3655
10	80mA	80	5560	0.2986	0.3837
11	110mA	25	4747	0.3417	0.3425
12	110mA	40	4754	0.3702	0.3742
13	110mA	60	5546	0.3447	0.3614
14	110mA	70	5681	0.3537	0.3779
15	110mA	80	5061	0.3426	0.3758
16	140mA	25	5178	0.3651	0.3616
17	140mA	40	5294	0.3755	0.3727
18	140mA	60	4818	0.3388	0.3743
19	140mA	70	5606	0.3516	0.3694
20	140mA	80	5216	0.3105	0.3509
21	170mA	25	4736	0.3383	0.3726
22	170mA	40	4882	0.3572	0.3760
23	170mA	60	5402	0.3454	0.3586
24	170mA	70	5656	0.3275	0.3536
25	170mA	80	5709	0.3067	0.3412
26	200mA	25	4611	0.3142	0.3626
27	200mA	40	5232	0.3747	0.3600
28	200mA	60	5260	0.3002	0.3542
29	200mA	70	5333	0.3469	0.3713
30	200mA	80	5128	0.2977	0.3453

Table 2 reports the experimental outcomes of the HHGSO-DL technique under varying aging. The results indicated that the lumen maintenance gets degraded with a rise in aging. In addition, the value of CCT gets improvised with an increase in aging.

Table 2 Experimental result of HHGSO-DL technique

Experimental data					
Case	**Aging**	**Lumen maintenance (%)**	**CCT (K)**	**X^a**	**Y^a**
Case_1	0h	100.00	2968	0.4335	0.4143
Case_2	240h	97.99	2974	0.4470	0.3732
Case_3	480h	96.70	3079	0.4492	0.3795
Case_4	720h	93.23	3079	0.4360	0.4233
Case_5	960h	91.14	3100	0.4446	0.3989
Case_6	1200h	87.90	3123	0.4257	0.3862
Case_7	1440h	84.01	3125	0.4233	0.4220
Case_8	1680h	80.44	3133	0.4208	0.3816
Case_9	1920h	77.09	3218	0.4129	0.3624
Case_10	2160h	74.26	3226	0.4208	0.3849

The SPD error norm analysis of the HHGSO-DL technique investigated varying levels of current and temperature as shown in Table 3. The results indicated that the HHGSO-DL technique reaches reduced values of SPD error norm. It is noticed that the SPD error norm values degrade with an increase in current and temperature values.

Table 3 SPD error norm analysis of HHGSO-DL technique under varying current and temperature

Current	**Temperature**				
	25°C	**40°C**	**60°C**	**70°C**	**80°C**
50mA	1.8625	2.8959	2.5575	1.7609	1.2701
80mA	1.0623	1.1103	0.8762	0.6549	0.5192
110mA	0.6047	0.5646	0.2984	0.4072	0.4350
140mA	0.4305	0.2934	0.2854	0.3871	0.4129
170mA	0.3615	0.2369	0.2074	0.2504	0.3188
200mA	0.3478	0.2150	0.1709	0.1663	0.2679

Table 4 reports the overall predictive accuracy results of the HHGSO-DL technique with different values of input current and case temperature. The results indicated that the HHGSO-DL technique has shown effectual outcomes in all cases. For instance, with input current of 50mA and case temperature of 25°C, the HHGSO-DL technique has obtained ΔCCT of 0.01592K and ΔXY^a of 0.00729. Concurrently, with input current of 50mA and case temperature of 70°C, the HHGSO-DL approach has attained ΔCCT of -0.02606K and ΔXY^a of 0.01279. Simultaneously, with input current of 50mA and case temperature of 70°C, the HHGSO-DL methodology has obtained ΔCCT of -0.02606K and ΔXY^a of 0.01279. Meanwhile, with input current of 80mA and case temperature of 80°C, the HHGSO-DL system has achieved ΔCCT of -0.00881K and ΔXY^a of 0.00707. Eventually, with input current of 110mA and case temperature of 25°C, the HHGSO-DL method acquired ΔCCT of -0.00018K and ΔXY^a of 0.00930.

Table 4 Prediction accuracy of HHGSO-DL technique with different input current and case temperature

Case No.	**Input current**	**Case Temperature**	**ΔCCT (K)**	**ΔXY^a**
1	50mA	25°C	0.01592	0.00729
2	50mA	40°C	-0.00123	0.00141
3	50mA	60°C	-0.01797	0.00357
4	50mA	70°C	-0.02606	0.01279
5	50mA	80°C	-0.02554	0.01241

6	80mA	25°C	0.01689	0.01014
7	80mA	40°C	0.00438	0.00523
8	80mA	60°C	-0.00320	0.00370
9	80mA	70°C	-0.00712	0.00208
10	80mA	80°C	-0.00881	0.00707
11	110mA	25°C	-0.00018	0.00930
12	110mA	40°C	0.00274	0.00063
13	110mA	60°C	-0.00513	0.00276
14	110mA	70°C	-0.00546	0.00687
15	110mA	80°C	-0.00861	0.00453
16	140mA	25°C	-0.00056	0.00487
17	140mA	40°C	-0.00689	0.00263
18	140mA	60°C	-0.00620	0.00109
19	140mA	70°C	-0.00824	0.00386
20	140mA	80°C	-0.00103	0.00300
21	170mA	25°C	-0.00919	-0.00043
22	170mA	40°C	-0.00572	-0.00222
23	170mA	60°C	-0.00706	0.00252
24	170mA	70°C	-0.00637	-0.00285
25	170mA	80°C	-0.00180	-0.00139
26	200mA	25°C	-0.01057	-0.00091
27	200mA	40°C	-0.00427	0.00221
28	200mA	60°C	-0.00080	0.00716
29	200mA	70°C	-0.00016	-0.00132
30	200mA	80°C	0.00105	-0.00041

To illustrate the better performance of the HHGSO-DL technique, a brief comparison study is made in Table 5 in terms of different measures [22]. Fig. 6 examines the SPD error norm results of the HHGSO-DL technique with the existing LSTM model. The results highlighted that the HHGSO-DL technique reaches reduced values of SPD error norm compared to the LSTM model. For instance, with case 2 and aging of 240hrs, the SPD error norm attains decreasing SPD error norm of 0.1362 while the LSTM model offers SPD error norm of 0.1450. Moreover, with case 4 and aging of 720hrs, the SPD error norm achieves reducing SPD error norm of 0.1432 while the LSTM algorithm offers SPD error norm of 0.1544. Similarly, with case 8 and aging of 1680hrs, the SPD error norm attains lesser SPD error norm of 0.1494 while the LSTM system provides SPD error norm of 0.1580. Likewise, with case 10 and aging of 2160hrs, the SPD error norm gains reduce SPD error norm of 0.1293 while the LSTM approach offers SPD error norm of 0.1396.

Table 5 Comparative analysis of HHGSO-DL approach with distinct measures

Case	Aging (hrs)	SPD error norm		Lumen maintenance		CCT (K)		XY^a	
		LSTM	HHGSO-DL	LSTM	HHGSO-DL	LSTM	HHGSO-DL	LSTM	HHGSO-DL
1	0	0.1482	0.1395	0.0000	0.0000	-0.0006	-0.0002	0.0003	0.0003
2	240	0.1450	0.1362	0.0040	0.0034	-0.0327	-0.0340	0.0138	0.0133
3	480	0.1456	0.1358	0.0158	0.0157	-0.0353	-0.0348	0.0180	0.0179
4	720	0.1544	0.1432	0.0310	0.0297	-0.0417	-0.0430	0.0239	0.0224
5	960	0.1652	0.1591	0.0723	0.0731	-0.0482	-0.0486	0.0281	0.0296
6	1200	0.1702	0.1595	0.0847	0.0848	-0.0480	-0.0466	0.0276	0.0271
7	1440	0.1682	0.1607	0.0789	0.0795	-0.0467	-0.0474	0.0260	0.0247
8	1680	0.1580	0.1494	0.0675	0.0662	-0.0566	-0.0562	0.0266	0.0251
9	1920	0.1447	0.1383	0.0473	0.0489	-0.0267	-0.0286	0.0155	0.0171
10	2160	0.1396	0.1293	0.0158	0.0145	-0.0191	-0.0196	0.0107	0.0096

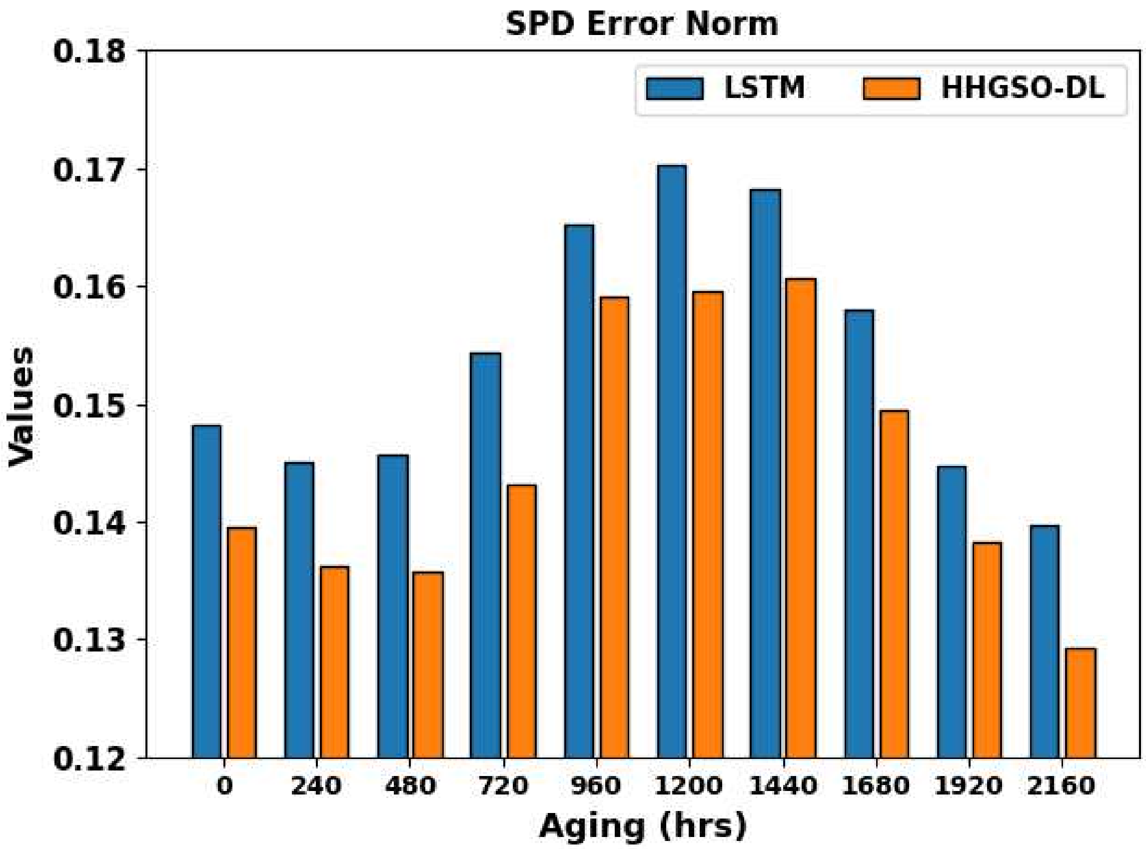

Fig. 6. SPD error norm analysis of HHGSO-DL approach with distinct aging

Fig. 7 inspects the lumen maintenance outcomes of the HHGSO-DL system with the existing LSTM approach. The outcomes demonstrated that the HHGSO-DL method reaches reduced values of lumen maintenance compared to the LSTM model. For instance, with case 2 and aging of 240hrs, the lumen maintenance gains minimal lumen maintenance of 0.0034 while the LSTM system provides lumen maintenance of 0.0040. Additionally, with case 4 and aging of 720hrs, the lumen maintenance accomplishes decreasing lumen maintenance of 0.0297 while the LSTM model offers lumen maintenance of 0.0310. Likewise, with case 8 and aging of 1680hrs, the lumen maintenance attains decreasing lumen maintenance of 0.0662 while the LSTM model offers lumen maintenance of 0.0675. Also, with case 10 and aging of 2160hrs, the lumen maintenance achieves lesser lumen maintenance of 0.0145 while the LSTM methodology offers lumen maintenance of 0.0158.

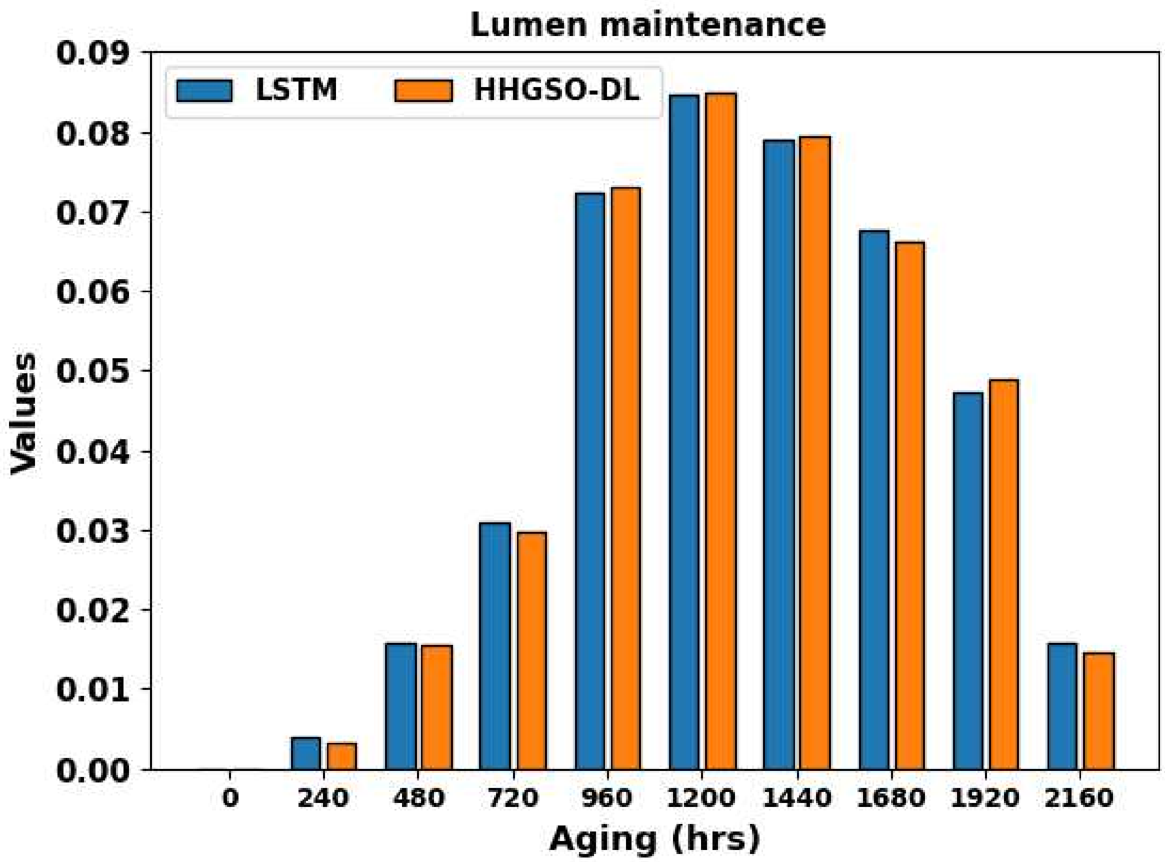

Fig. 7. Lumen maintenance analysis of HHGSO-DL approach with distinct aging

Fig. 8 showcases XY^a outcomes of the HHGSO-DL system with the existing LSTM algorithm. The outcomes demonstrated that the HHGSO-DL approach gains lower values of XY^a compared to the LSTM system. For instance, with case 2 and aging of 240hrs, the XY^a attains decreasing XY^a of 0.0133 while the LSTM method offers XY^a of 0.0138. Next, with case 4 and aging of 720hrs, the XY^a attains decreasing XY^a of 0.0224 while the LSTM algorithm offers XY^a of 0.0239. In the meantime, with case 8 and aging of 1680hrs, the XY^a attains decrease XY^a of 0.0251 while the LSTM approach provides XY^a of 0.0266. Lastly, with case

10 and aging of 2160hrs, the XY^a realizes minimum XY^a of 0.0096 while the LSTM system offers XY^a of 0.0107.

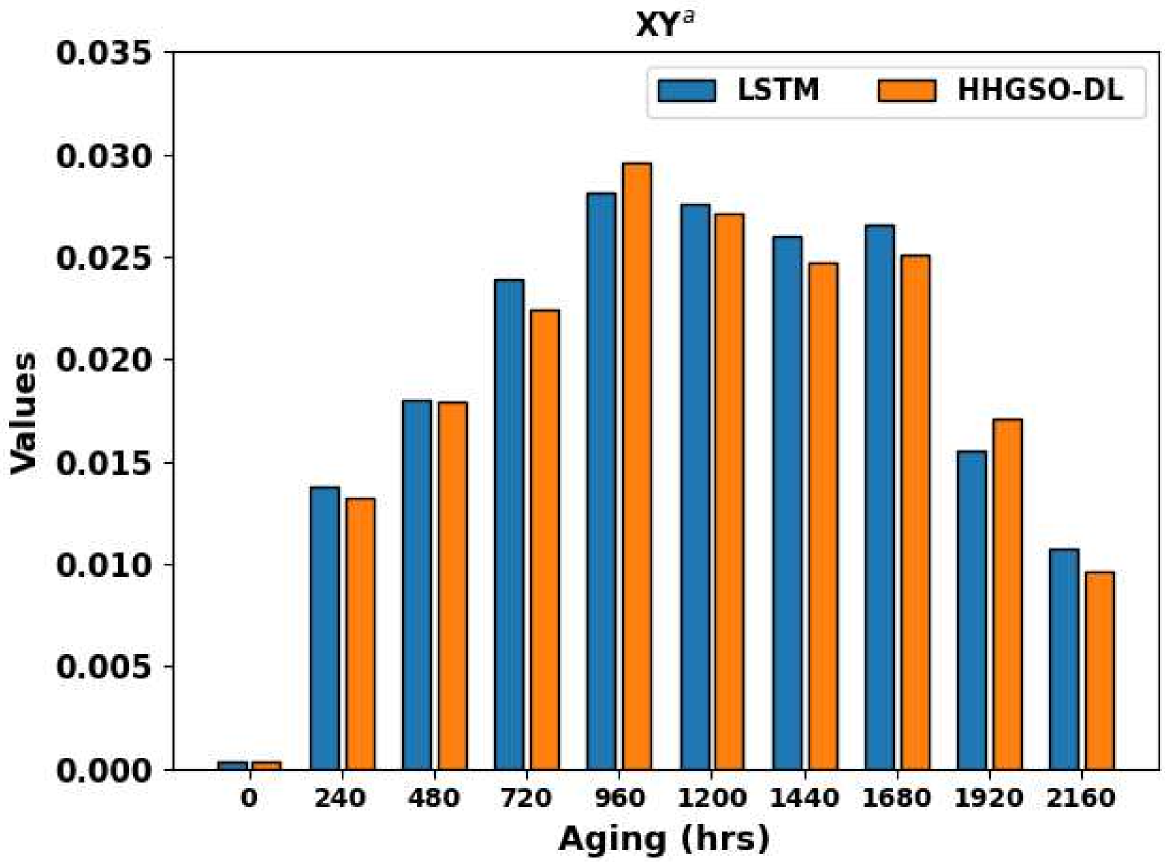

Fig. 8. XY^a analysis of HHGSO-DL approach with distinct aging

These results stated that the HHGSO-DL technique showed better performance over the existing model under several dimensions.

5. Conclusion

In this study, we have developed a novel HHGSO-DL technique for LED driver system design. The presented HHGSO-DL technique is majorly intended for the determination of the empirical relationship among the design parameters, thermal aging loading, and luminous outcomes of the LED product. In the presented HHGSO-DL technique, the HHGSO with BiLSTM model can be employed to examine the empirical relationship and its hyperparameters can be tuned by the HHGSO algorithm. The experimental result analysis of the HHGSO-DL technique can be inspected on LED chip packaging and LED luminaire with thermal aging loading. The extensive results demonstrate the promising performance of the HHGSO-DL technique over other state of art approaches. In future, advanced DL models can be integrated into the

HHGSO-DL technique for enhanced predictive outcomes in the design of LED driver systems.

Declarations

Data Availability Statement: The manuscript has no associated data.

Competing Interests and Funding: The authors did not receive support from any organization for the submitted work.

Human Participants and/or Animals: Not applicable

Conflict of Interest: The authors have expressed no conflict of interest.

References

[1] Yin, Y., Mao, J. and Liu, R., 2022. Multivariable-Feedback Sliding-Mode Control of Bidirectional DC/DC Converter in DC Microgrid for Improved Stability with Dynamic Constant Power Load. *Electronics*, *11*(21), p.3455.

[2] Burcea, F., Tannir, D. and Graeb, H.E., 2019. Fast SPICE-Compatible Simulation of Low-Power On-Chip PWM DC–DC Converters With Improved Ripple Accuracy. *IEEE Transactions on Power Electronics*, *35*(8), pp.8173-8185.

[3] Bosich, D., Giadrossi, G., Pastore, S. and Sulligoi, G., 2021. Weighted Bandwidth Method for Stability Assessment of Complex DC Power Systems on Ships. *Energies*, *15*(1), p.258.

[4] Meng, X., Jia, Y., Xu, Q., Ren, C., Han, X. and Wang, P., 2022. A Novel Intelligent Nonlinear Controller for Dual Active Bridge Converter with Constant Power Loads. *IEEE Transactions on Industrial Electronics*.

[5] Rios, C.S., Nogueira, F.G., Torrico, B.C. and Junior, W.B., 2021. Robust control of a DC-DC three-port isolated converter. *Transactions of the Institute of Measurement and Control*, *43*(12), pp.2658-2675.

[6] Zhang, X., Zhong, Q.C., Kadirkamanathan, V., He, J. and Huang, J., 2018. Source-side series-virtual-impedance control to improve the cascaded system stability and the dynamic performance of its source converter. *IEEE Transactions on Power Electronics*, *34*(6), pp.5854-5866.

[7] Hajihosseini, M., Andalibi, M., Gheisarnejad, M., Farsizadeh, H. and Khooban, M.H., 2020. DC/DC power converter control-based deep machine learning techniques: Real-time implementation. *IEEE Transactions on Power Electronics*, *35*(10), pp.9971-9977.

[8] Sabir, A., 2019. A PLL-free robust control scheme with application to grid-connected fuel cell DGs under balanced and unbalanced conditions. *Sustainable Energy Technologies and Assessments*, *31*, pp.64-76.

[9] Thounthong, P., Nahid-Mobarakeh, B., Pierfederici, S., Mungporn, P., Bizon, N. and Kumam, P., 2020, October. Hamiltonian Control Law Based on Lyapunov–Energy Function for Four-Phase Parallel Fuel Cell Boost Converter. In *2020 International Conference on Power, Energy and Innovations (ICPEI)* (pp. 255-260). IEEE.

[10] Poorali, B., Adib, E. and Farzanehfard, H., 2016. A single-stage single-switch soft-switching power-factor-correction LED driver. *IEEE Transactions on Power Electronics,* 32(10), pp.7932-7940.

[11] S. Sánchez, A.G., Perez-Pinal, F.J. and Espinosa-Calderón, A., 2022. Optimization and Its Implementation Impact of Two-Modes Controller Fractional Approximation for Buck Converters. *Micromachines*, *13*(10), p.1600.

[12] Xu, Q., Yan, Y., Zhang, C., Dragicevic, T. and Blaabjerg, F., 2019. An offset-free composite model predictive control strategy for DC/DC buck converter feeding constant power loads. *IEEE Transactions on Power Electronics*, *35*(5), pp.5331-5342.

[13] Kreiss, J., Bodson, M., Delpoux, R., Gauthier, J.Y., Trégouët, J.F. and Lin-Shi, X., 2021. Optimal control allocation for the parallel interconnection of buck converters. *Control Engineering Practice*, *109*, p.104727.

[14] Junior, F.A.D.C.A., Bessa, I., Pereira, V.M.B., da Silva Farias, N.J., de Menezes, A.R., de Medeiros, R.L., Chaves Filho, J.E., Lenzi, M.K. and da Costa Júnior, C.T., 2020. Fractional Order Pole Placement for a buck converter based on commensurable transfer function. *ISA transactions*, *107*, pp.370-384.

[15] Zhang, F., Zhang, Z., Xiao, S., Xie, K., Ni, J., Gu, H., Wu, Y., Ning, Y. and Xia, Q., 2021. Design and Implementation for the High Voltage DC-DC Converter of the Subsea Observation Network. *Journal of Marine Science and Engineering*, *9*(7), p.712.

[16] Iam, I.W., Hoi, I.U., Huang, Z., Gong, C., Lam, C.S., Mak, P.I. and Martins, R.P., 2020. Constant-frequency and non-communication-based inductive power transfer converter for battery charging. *IEEE Journal of Emerging and Selected Topics in Power Electronics*.

[17] Liao, J., Guo, C., Huang, Y., Qiu, G., Zhou, N. and Wang, Q., 2022. Active Damping Control of Cascaded DC Converter in DC Microgrids Based on Optimized Parallel Virtual Resistance. *IEEE Journal of Emerging and Selected Topics in Industrial Electronics*.

[18] Salimi, M., 2018. A Novel Method on Nonlinear and Adaptive Control of Buck DC to DC Converter.

[19] Sanchez, R.O., Rumbo Morales, J.Y., Ortiz Torres, G., Pérez Vidal, A.F., Valdez Resendiz, J.E., Sorcia Vázquez, F.D.J. and Nava, N.V., 2022. Discrete State-Feedback Control Design with D-Stability and Genetic Algorithm for LED Driver Using a Buck Converter. *International Transactions on Electrical Energy Systems*, *2022*.

[20] Peng, T., Zhang, C., Zhou, J. and Nazir, M.S., 2021. An integrated framework of Bi-directional long-short term memory (BiLSTM) based on sine cosine algorithm for hourly solar radiation forecasting. *Energy*, *221*, p.119887.

[21] Ekinci, S., Hekimoğlu, B. and Izci, D., 2021. Opposition based Henry gas solubility optimization as a novel algorithm for PID control of DC motor. *Engineering Science and Technology, an International Journal*, *24*(2), pp.331-342.

[22] Yuan, C.C., Fan, J. and Fan, X., 2021. Deep machine learning of the spectral power distribution of the LED system with multiple degradation mechanisms. *Journal of Mechanics*, *37*, pp.172-183.